Analyst

Coherent anti-Stokes Raman scattering imaging of microcalcifications associated with breast cancer

Journal:	*Analyst*
Manuscript ID	AN-ART-10-2020-001962.R1
Article Type:	Paper
Date Submitted by the Author:	14-Nov-2020
Complete List of Authors:	Petrov, Georgi; Texas A&M University, Arora, Rajan; Lam Research Yakovlev, Vladislav; Texas A&M University, Biomedical Engineering

ARTICLE

Coherent anti-Stokes Raman scattering imaging of microcalcifications associated with breast cancer

Georgi I. Petrov,[a] Rajan Arora [b] and Vladoslav V. Yakovlev [*a,c,d]

Received 00th January 20xx,
Accepted 00th January 20xx

DOI: 10.1039/x0xx00000x

Chemical imaging of calcifications was demonstrated in the depth of a tissue. Using long wavelength excitation, broadband coherent anti-Stokes Raman scattering and hierarchial cluster analysis, imaging and chemical analysis was attained 2-mm below the skin level in a model system. Applications to breast cancer diagnostics and imaging are discussed together with the methods to further extend the depth and improve the spatial resolution of chemical imaging.

Introduction

Chemical imaging has revolutionized our ability to study complex chemical processes occurring in microscopic world with unprecedented details [12]. It is an exciting emerging analytical approach that integrates conventional imaging and spectroscopy to attain spatial and spectral information of the sample. Chemical species are identified by acquiring spatially resolved spectra, which enable the visualization of chemical's distribution within the sample. Chemical mapping techniques have tremendous applications in several disciplines including chemistry, material science, medicine and pharmacy, food science and agriculture, medical science, and biology [345]. Particularly, in biology, chemical imaging is emerging as a powerful tool for in vivo investigation of biological samples [6 7]. Since chemical properties of any tissue strongly depend on the spatial organization of complex biological macromolecules and their interactions, it can be used as a method of detecting and quantifying malignancy in biological tissues [8]. However, the application of chemical imaging techniques to cancer tissues outside the research laboratory is greatly limited by a number of factors. Firstly, imaging living tissues often requires the introduction of specific labels to achieve a reliable and reproducible contrast[9]. Modalities, which don't rely on contrast-enhancing agents, are often limited by a poor signal quality, a lack of chemical specificity, and sensitivity, which results in long acquisition times; hence, many of the imaging modalities can be hardly used for chemically-specific real time imaging[8]. In this report, we are describing a non-invasive chemical imaging technique that can potentially address the limitations of current clinical diagnostic procedures in breast cancer and has the potential to provide real time chemically specific information.

Breast cancer is a major disease affecting one in 8 women in both developing and developed countries [9]. With the highest annual incidence rate in the US, it is the second-most common cause of cancer death[10]. In most of the cases, specks of calcium, also known as microcalcifications, are found in the affected area and are considered as one of the first mammographic signs associated with breast cancer[11]. These microcalcifications found in the area of rapidly dividing cells are separable into two types based on their predominant chemical constituent. More common type of microcalcification, calcium phosphate (Type II) (CaP), appears dark blue in routine hematoxylin and eosin stained tissue sections and is frequently associated with infiltrating and intraductal carcinoma[13]. Conversely, Type I microcalcifications are colourless birefringent crystals of calcium oxalate (CaO_x), which are exclusively associated with benign lesions or, at the most, with lobular carcinoma[13]. An accurate identification of these microcalcifications plays a key role in early detection of breast cancer. It will not only help to reduce the number of benign tissue biopsies and associated with them high medical cost, but will also save patients from unnecessary surgeries and post-surgical trauma. In the same time, it will also help to quickly screen those biopsies for calcifications during the ongoing surgery helping to identify tumour margins. Hence, it becomes extremely important to develop fast, cost effective and unambiguous methods to accurately identify and image such microcalcifications.

Significant research efforts have been focused on breast cancer detection resulting in the emergence of new imaging techniques over the past several years [14]. A gold standard for breast cancer screening, mammography is a traditional imaging technique that employs X-rays to probe density changes in the breast tissues [15]. However, these density changes are not uniquely correlated with a breast cancer. Moreover, a low signal contrast, a risk of repeated exposure to a harmful ionizing radiation, and a relatively low spatial resolution limits this

[a] Department of Biomedical Engineering, Texas A&M University, College Station, TX 77843, USA.
[b] Present address Lam Research, Inc. 11361 SW Leveton Drive, Tualatin, OR 97062, USA.
[c] Department of Physics and Astronomy, Texas A&M University, College Station, TX 77843, USA
[d] Department of Electrical and Computer Engineering, Texas A&M University, College Station, TX 77843, USA.

technique for screening purposes rather than serving as a diagnosis tool [15,16]. As a result, the breast tissue, which is found positive by either clinical breast examination or X-ray mammography, is always biopsied and analysed by pathologist [17]. The respective analysis and the interpretation of those biopsies is often a time-consuming process and may require multiple biopsies due to a subjective analysis. Other imaging techniques, such as computed tomography (CT), magnetic resonance imaging (MRI), and positron emission tomography (PET) are less prone to sampling errors and are helpful in providing information about the local anatomy [19,19]. These techniques do not provide with detailed information about the biochemical composition of lesions and are generally of low resolution, causing small calcifications to go undetected [20]. Optical spectroscopic techniques are also under investigation for breast cancer imaging and are known to provide morphological details with subcellular spatial resolution [21,22]. Unlike the previous techniques, optical spectroscopic techniques have the advantage of immediate chemical information and, hence, can be used for a real-time imaging and identification of microcalcifications. Several studies report on ex-vivo detection of cancer tissue by fluorescence spectroscopy [24,24]. Fluorescence microscopy, being extremely sensitive down to a single molecule detection and imaging, relies on the presence of intrinsic or extrinsic fluorophore to achieve the desired chemical selectivity. However, this chemical contrast is greatly affected by the bleaching, and the phototoxicity of those external markers is always questionable. This problem could be addressed by conventional vibrational microscopies based on the infrared and Raman spectroscopies. Despite of being non-invasive and label-free, these methods, however, lack the sensitivity required for a rapid tissue imaging. For example, imaging capabilities of infrared microscopy are significantly affected by the strong water absorption, which is mostly the case with biological tissues, and a low spatial resolution associated with the long excitation wavelength. Since water molecules are poor Raman scatterers, Raman spectroscopic probing of tissues can be done even in the presence of water. Recently, several groups have demonstrated successful discrimination of breast cancer cells and tissues using Raman spectroscopy [22,25,26]. Unfortunately, practical implementation of Raman spectroscopy to rapid tissue imaging is hampered by long integration times and large fluorescence background. On the other hand, as a nonlinear optical analogue of spontaneous Raman, spectroscopy based on coherent anti-Stokes Raman scattering (CARS), can overcome most of the problems associated with conventional Raman spectroscopy [5]. In CARS spectroscopy, the signal is generated by the stimulated coherent excitation of many vibrational oscillators, which assures much stronger signal than that of a conventional Raman spectroscopy [27]. In addition, the chemical contrast is provided by the intrinsic molecular vibrations which circumvent the need of extrinsic labels and overcome the complications associated with photobleaching [28]. The anti-Stokes signal is blue-shifted from the pump and Stokes frequencies thus the detected signal is always free from fluorescence interference. Last but not the least, the nonlinear dependence of the CARS signal on the incident intensity assures signal to be generated only from focal area where the excitation density is the highest, giving CARS microscopy its 3D sectioning capability [30,31]. Despite of these advantages, the complex contribution of resonant and non-resonant part of the signal makes quantitative analysis a challenging task. In addition, high cost associated with lasers and complexity of the experimental set up limits the use of this technique for biomedical applications. However, with careful system design, understanding of the contrast mechanism, emergence of retrieval algorithms, and the development of advanced diode-pumped laser sources, these limitations can be addressed with minimal complexity. For these reasons, we have investigated CARS spectroscopy as a potential clinical tool for detection, imaging and identification of microcalcifications.

CARS is a nonlinear four wave mixing technique in which molecular vibrations are driven coherently through stimulated excitation by laser pulses. In this process, a pump beam with frequency ω_1 combines coherently with a Stokes beam at frequency ω_2, and, while interacting with the sample, they generate a signal at frequency ω in the phase matched direction [31]. When the frequency difference between the pump and Stokes beams matches a vibrational energy level in the sample, this process is resonantly enhanced and the detected signal rises tremendously. Signal intensity in the CARS spectroscopy is proportional to the square modulus of the third order nonlinear susceptibility $\chi^{(3)}$. This signal is a complex sum of resonant electronic contributions arising from different vibrational modes and a non-resonant electronic contribution due to a number of interfering four-wave mixing processes; hence, it carries a complex shape:

$$I_{CARS}(\omega) = I_{CARS}(2\omega_1 - \omega_2) \propto \left|\chi_{NR}^{(3)} + \chi_R^{(3)}(\omega)\right|^2 \quad (1)$$

$$\chi_R^{(3)}(\omega) = \sum_j \frac{A_j}{\Omega_j - (\omega_1 - \omega_2) - i\Gamma_j} \quad (2)$$

where A_j, Ω_j and Γ_j are the amplitude, linewidth and frequency of the j^{th} Raman mode. Here, the non-resonant part if real and doesn't depend on the frequency, which is generally true for the excitation far enough from the electronic resonance. It has been shown that $Im(\chi^{(3)})$ is proportional to the strength of spontaneous Raman signal and provides direct quantitative analysis of molecular concentrations [32,33] . Several methods have been proposed and developed to minimize the non-resonant background in CARS spectroscopy and imaging. Those include polarization-sensitive detection[35], phase mismatching techniques [35], time-delayed CARS [36], epi-CARS [37] and phase retrieval methods [38,39] . While instrumentation approaches are based on additional complexity of the experimental setup, the phase retrieval methods are very attractive because they operate with the existing CARS spectral data and get the most information out of those spectral data without any modification to existing instrumentation. In some sense, they are based on non-linear analogues of Kramer-Kroning relationship [40]. It has been shown that the method based on Maximum Entropy Model (MEM) can retrieve the imaginary part of $\chi^{(3)}$ without any *a priori* information about vibrational bands or any further modifications of the experimental setup [38,41,42]. In this approach, the acquired CARS spectrum is fitted with its Maximum Entropy

(ME) estimation leading to direct Raman spectrum, which can be then used for analysis.

In this report, we employed CARS microspectroscopy to detect, image and characterize the chemical/morphological composition of microcalcifications in a model system mimicking thick breast tissue. This system fairly represents thick histopathological slices and, thus, can be implemented for analysis of thick biopsy samples. CARS spectra acquired at each spatial location, were retrieved, and Raman spectra were used to analyse the chemical content and a spatial distribution of chemicals. Cluster analysis, which separates clusters based on the dissimilarity between spectra was implemented to discriminate regions of different calcifications in a CARS image. The reported data demonstrate the efficiency and great untapped potential of these statistical tools and open the path for future clinical diagnostic applications.

Experimental setup

While stimulated Raman scattering (SRS) is currently largely used for fast chemical imaging, CARS microspectroscopy offers several features which makes it attractive for a given specific application. In particular for chemical analysis, the broadband spectrum is important, and CARS microspectroscopy allows simultaneous spectral acquisition from 400 to 4000 cm^{-1}. To minimize tissue photodamage and to facilitate deeper penetration of the incident light, longer incident wavelength is preferred [43][44]. By using the 1064 nm radiation as the pump beam, the detected signal falls into high-sensitivity region for conventional Si detectors, while for SRS spectroscopic imaging

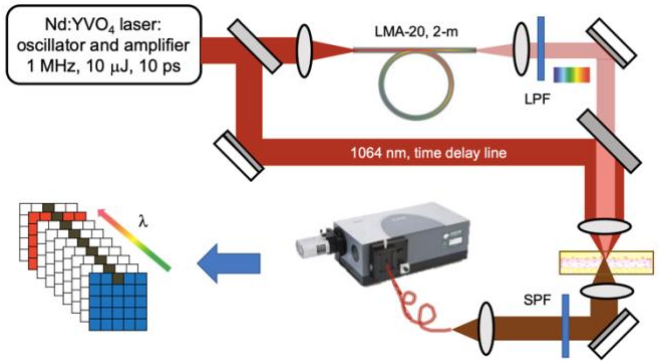

Figure 1. Experimental setup for CARS microspectroscopy. Homebuilt Nd:YVO4 oscillator/amplifier operates at 1 MHz and delivers transform limited pulses with a pulse duration of 10-ps. 10% of the output is sent into a specialized fibre to generate white-light continuum. A portion of this supercontinuum above 1100 nm is selected using a set of long-pass filter (LPF). The rest of the power is passing through a time-delay line to be combined with the broadband Stokes beam to be focused into a sample. The CARS signal is collected in forward propagating direction and is filtered out using a series of short-pass filters (SPF) to be sent to spectrometer for detection. Hyperspectral data are then collected and analysed using CytoSpec, Inc software.

it would require the use of more expensive InGaAs detectors. The use of a white-light continuum source as the Stokes beam significantly simplifies the overall system design and reduces the cost of the system [45], while a sophisticated wavelength tuning system is typically needed for spectroscopic SRS imaging [46][47][48]. The strength of the CARS signal is proportional to the product of three incident intensities (i.e. effectively is proportional to the third power of the incident intensity), as compared to SRS, which is proportional to the product of pump and Stokes intensities (i.e. effectively is proportional to the second power of the incident intensity). This provides a better discrimination against out of focus signal as it was demonstrated in the cased of three-photon absorption imaging [49]. Those factors led us to use CARS microspectroscopy for imaging calcifications. The experimental setup is depicted in Fig. 1 and is described in greater details in Ref. [50]. In brief, the fundamental output of a picosecond, diode-pumped Nd:YVO_4 oscillator-amplifier system was used to serve both the pump and probe beam in the CARS interaction, while the broadband continuum generated in a special single-mode fibre (LMA-20; Thorlabs, Inc.) [51], was employed as the Stokes beam. Two beams were combined together by means a dichroic mirror. To facilitate a better discrimination against out of focus signals, two beams were slightly offset against each other to minimize their overlap outside the focal area. Monte Carlo simulations [52] were used to optimize the geometry of focusing for any given microscopic setting. In a typical configuration, we used long working distance near-IR microscope with a numerical aperture of 0.67 (OptoSigma, Inc.; PAL-50-NIR-HR-LC00) to focus both beams onto the sample. The generated light was collected using a high-numerical (NA=0.76; Thorlabs, Inc. ACL50832U-B, AR coated for 650-1000 nm) and through a set of short-pass and dichroic filter was directed to a 1/3-meter imaging spectrometer (Andor Tech, Inc; Shamrock) with the attached deep depletion TE-cooled CCD optimized for the near-IR detection (Andor Tech, Inc.; Newton BEX2-DD). For each set of measurements, we collected a reference CARS spectrum from a fused silica slide to compensate for the system transmission and a long-term drift, if any, of the white-light continuum spectra. The acquisition time was set at 100-ms for imaging through scattering tissue and 10 ms for imaging pure substances. The incident power was maintained at the level of 10 mW to keep the temperature rise within several degrees [53][54].

Spontaneous Raman spectra were taken using a home built confocal Raman microscope equipped with a 50-mW intracavity doubled Nd:YVO_4 laser excitation source ($\lambda = 532nm$). The light scattered from the sample was collected with a high numerical aperture objective lens (Nikon, Inc.; 60X water immersion, fluorite aberration corrected objective lens with a numerical aperture, NA=1.0) to maximize the collection efficiency of the signal. Raman signals were captured in a back-scattering geometry, filtered with a notch filter and directed to a high-throughput spectrometer (Jobin-Yvon; Triax-320), where the spectrally resolved signal was detected with a liquid-nitrogen-cooled CCD camera (Jobin-Yvon; CCD 3000). Typical spectral resolution in the spectral region of interest was 3 cm^{-1}, and the reproducibility of the Raman peaks' position was within 0.5 cm^{-1}. Samples were illuminated with 50-mW laser for 100 s and the collected spectra were averaged over 5 accumulations. Calcium oxalate hydrate ($CaC_2O_4 \cdot (H_2O)_x$) and calcium phosphate hydroxide ($3Ca_3(PO_4)_2 \cdot Ca(OH)_2$) (suspension in 1mM phosphate buffer, pH 6.8) were purchased from Sigma-Aldrich, Inc. For all the described measurements, a 1:1 mixture of both types of calcifications was prepared. To date, most of the experiments have been performed either on excised human breast tissue or

on a chicken breast phantom. Chicken tissue, which was purchased in a local supermarket (Pick'n-Save, Kroger, Inc.), was used in the model due to its relative homogenous nature. However, we do recognize that the actual human breast tissue is made of fat tissue with stromal and epithelial tissue in it, which is actually less dense than chicken tissue. Therefore, our spectra from chicken tissue do not show all the Raman bands associated with a human breast tissue, but they do represent a significant part of it. To demonstrate the full potential of CARS microspectroscopy for breast cancer screening, we performed two sets of experiments: one with a sample containing microcalcifications only and the other – with microcalcifications sandwiched in between chicken tissue (about 2 mm inside the tissue). The aim of the first experiment was to identify and localize both microcalcifications in a mixture form. The second experiment was performed to mimic the actual scenario i.e. microcalcifications present in a breast tissue substantially deep inside the tissue.

To analyse hyperspectral images, we utilized a commercial software package (CytoSpec, Inc.; version 1.4.02) to perform hierarchical cluster analysis. We used D-values as a measure of similarity between the spectra, and Ward's algorithm to further combine the clusters after first iteration. This combination in spectroscopy is known to construct the most homogeneous groups [5556].

Experimental results

To demonstrate the potential of the MEM phase retrieval procedure in CARS microspectroscopy for breast cancer diagnostics, the technique was first applied to identify the chemical composition of Type I and Type II calcifications. In Fig. 2, the CARS spectra and the retrieved Raman spectra of both Type I and II calcification are shown. For a reference, Fig. 2 also shows the respective spontaneous Raman spectra. The characteristic Raman bands due to the C=O symmetric stretching vibration are observed at 1464 and 1490 cm^{-1} in the case of Type I calcification [57]. In the case of Type II calcifications, totally symmetric stretching mode (ν_1) of the tetrahedral PO_4 group (P–O bond) is observed at 961 cm^{-1} [5859]. Other prominent Raman lines appearing at 899, and 1631 cm^{-1} (not shown in the Fig. 2) for Type I calcifications are assigned to be C–C stretching, and C=O asymmetric stretching, respectively[57]. It should be noted that CARS spectra were converted to the corresponding Raman spectra without any a priori information about the Raman spectra.

The rapid imaging capability of CARS microspectroscopy readily allows us to map quantitatively the spatial and chemical variations of calcifications. For CARS imaging, the prepared samples were scanned over $100 \times 100\ \mu m^2$ area with a $1\ \mu m$

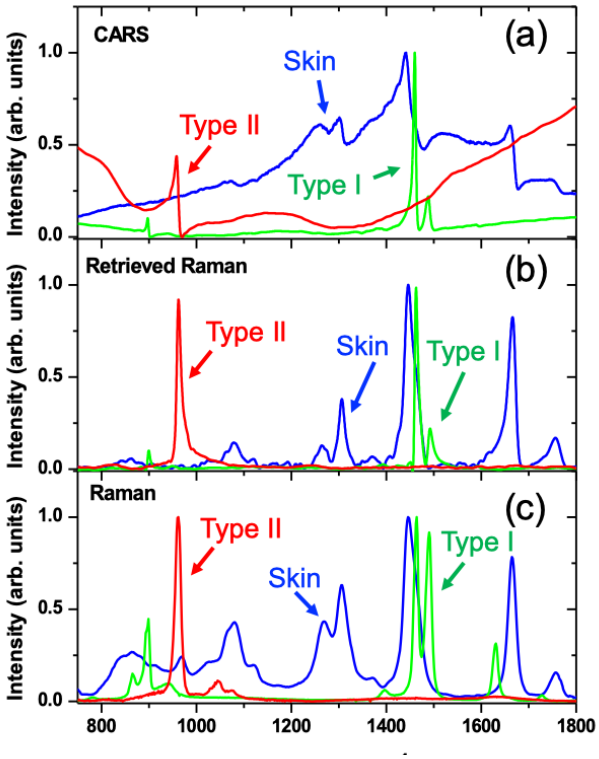

Figure 2. Experimentally measured CARS (a) and calculated Raman spectra retrieved from CARS spectra (b), as compared to spontaneous Raman spectra (c) for Type I and Type II calcifications and skin.

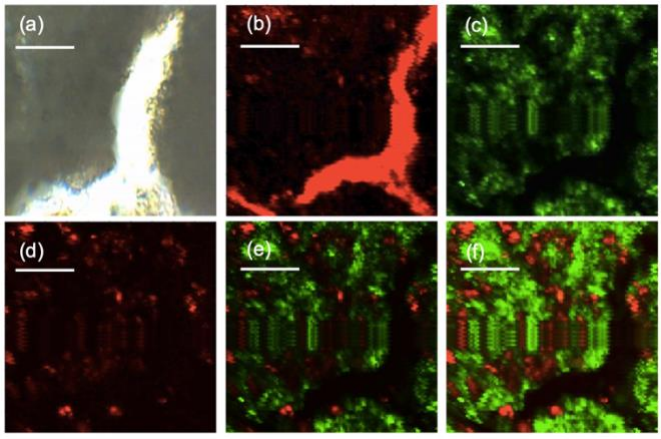

Figure 3. CARS spectral Imaging: (a) bright field image of the 1:1 mixture of Type I and II calcification, (b) CARS image away from any vibrational mode, (c) CARS image of Type I calcifications (C–C stretching mode), (d) CARS image of Type II calcifications (symmetric stretching mode (ν_1) of tetrahedral PO_4 group), (e) colocalized CARS image, and (f) colocalized retrieved Raman image of the mixture. Scale bar for all the images is 25 μm.

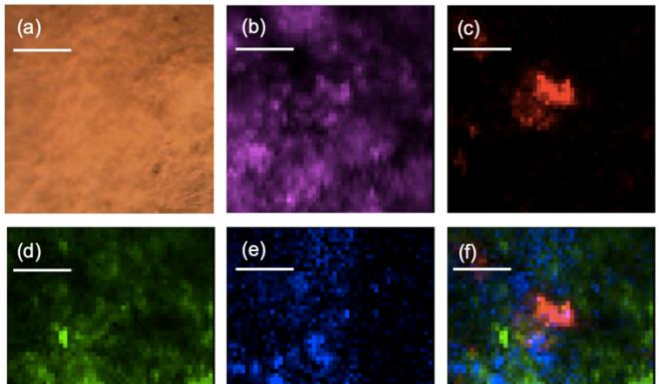

Figure 4. CARS spectral imaging through tissue: (a) bright field optical image of calcifications sandwiched between skin tissue, (b) CARS image away from any vibrational mode, (c) CARS image of Type II calcifications (symmetric stretching mode (ν_1) of tetrahedral PO_4 group), (d) CARS image of Type I calcifications (C–C stretching mode), (e) CARS image of skin tissue (scissor mode at around 1480 cm^{-1}), (f) pseudo-colour CARS image. Scale bar for all the images is 25 μm.

step size in both directions. From each and every point, an equivalent Raman spectrum was retrieved using the retrieval procedure[40]. Optical images of the scanned area for both the samples are shown in Fig. 3a and Fig. 4a for reference and, clearly, do not provide any meaningful information about microcalcifications and their distribution. The C–C stretching vibration of the Type I microcalcifications, the symmetric stretching mode (ν_1) of the tetrahedral PO_4 group of the Type II microcalcifications, and methylene scissor deformation of chicken tissue were used to visualize the chemical distribution of both the samples. Fig. 3 shows the CARS images of the background (which is taken away from any vibrational mode of the mixture), Type I, and Type II calcifications. Fig. 4 also shows image corresponding to the chicken tissue. In addition, a co-localized CARS image and a co-localized retrieved Raman image of two calcifications are shown in Fig. 3e,f and Fig. 4f. We demonstrate the power of hierarchical cluster analysis first for the mixture sample. On the basis of the connecting distances three distinctive clusters were defined. The final results of the procedure reported in the form of average spectra for each cluster, cluster image, and dendrogram are shown in Fig. 5. A dendrogram shows the hierarchical relationship between objects and indicates the order in which the clusters were joined. The length of the connecting lines reflects the distance between the clusters. The first cluster contains Raman

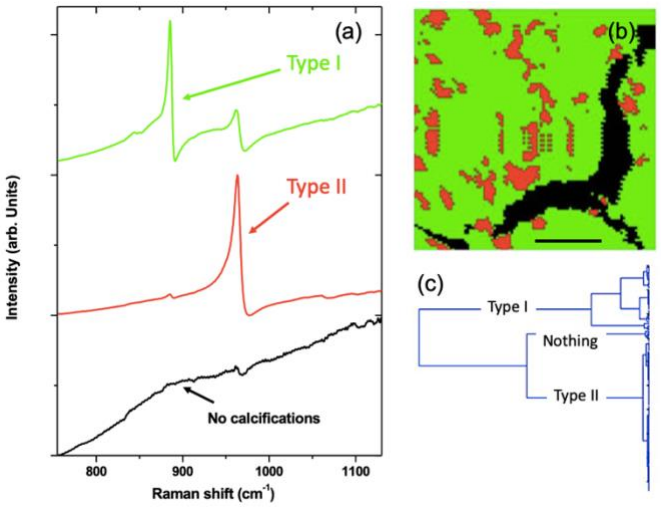

Figure 5. Cluster analysis of 1:1 mixture of calcifications: (a) average CARS spectra of three most common classes, (b) cluster image: green colour indicates cluster corresponding to Type I calcifications, red – Type II calcifications and black – empty spaces; scale bar is 25 μm, (c) dendrogram.

signatures corresponding to predominantly Type I calcification and the corresponding average spectrum (Fig. 5 (a)) clearly shows that the Type I is the prevalent component in the cluster. The second cluster mainly specifies the Type II calcification, and the average spectrum corresponding to the last cluster does not show any Raman bands and hence represents the region where calcifications are not present. The cluster image (Fig. 5 (b)) clearly shows the distribution of all the clusters in a CARS image. Hence cluster analysis proved to be a highly selective and convenient method to classify microcalcifications in CARS image.

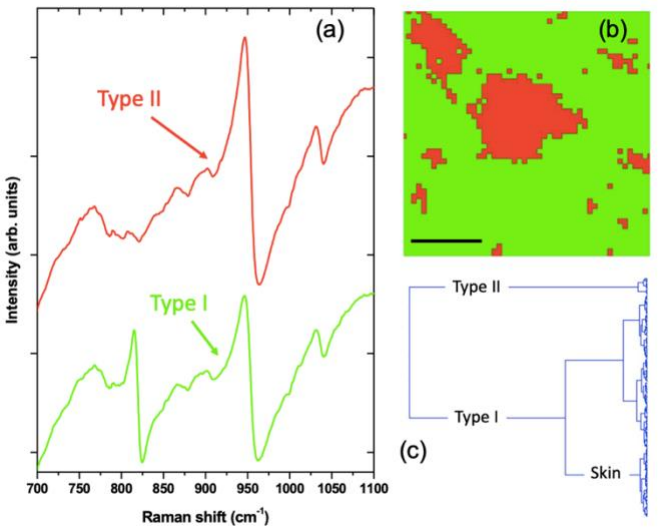

Figure 6. Cluster analysis of calcifications in deep tissue: (a) average CARS spectra of two most common clusters, (b) cluster image: green colour indicates cluster corresponding to Type I calcifications, red – Type II calcifications; scale bar is 25 μm, (c) dendrogram.

Similar analysis was performed for images of microcalcifications buried in skin tissue. Those results are depicted in Fig. 6. Fig. 6b shows cluster image, where only two clusters are selected to highlight the areas associated with Type II calcifications. Clearly, the area occupied by those calcifications is significantly larger than the one identified in Fig. 4. We attribute this to a simple fact that intensity measurements at a single Raman/CARS line provide information convoluted with the signal scattering properties, which can be drastically different for different locations, while cluster analysis considers the full spectral information and attempts to distinguish different chemical structures. If more clusters are used, we can separately distinguish areas predominantly occupied by skin tissue (low concentration of either calcification) and grade the areas based on the dominant presence of calcification; however, significant improvement in the signal-to-noise quality is required for an accurate analysis. Fig. 6a shows CARS spectra of two individual clusters. While those spectra appear to have a good signal-to-noise ratio, they actually represent the integrated CARS spectra over the whole cluster, which improves the overall quality of those spectra.

Discussion

Nonlinear Raman spectroscopy imaging is a powerful spectroscopic technique to provide chemical imaging in biological tissues. While significant efforts are devoted to make such imaging faster, we point that CARS microspectroscopy also provides a unique (both with respect to Raman and SRS imaging) capability of distinguishing chemical species in the depth of a tissue. In our demonstrated application, we were able to successfully image calcifications buried at the depth of about 2-mm inside a skin tissue in a model system. We also showed that hyperspectral imaging is essential for identifying chemical species. There are several potential ways for improvement, which are currently under way. Earlier, we have

demonstrated the successful application of adaptive optics for focusing light through the scattering tissue [6061], and in the next generation of optical instrumentation for CARS microspectroscopy we plan to implement it for deeper penetration depth and sharper focusing. Preliminary results indicate that, at least, comparable image quality is possible at the twice the depth reported here, when a spatial light modulator is used at the input of the microscope. Three-dimensional imaging is the ultimate goal; however, the current software limitation didn't allow us to process hyperspectral images larger than 10,000 spatial points, that is why we limited ourselves to two-dimensional imaging. Finally, the spatial resolution can be improved through structured light illumination [62], and we plan to explore this approach in our forthcoming studies focused on characterizing and improving spatial resolution imaging in the depth of scattering tissues.

Conclusions

In conclusion, differences in the chemical composition, which are not seen in the optical image, become directly apparent in both CARS and retrieved Raman images, which can be enhanced by cluster analysis. This can lead to the true concentration measurements of chemical compounds in the bulk of a living tissue and can be potentially applied for live-animal imaging, if the detection can be properly designed for a backscattered light collection. Our results clearly demonstrate the combined potential of CARS spectroscopy, MEM-based phase retrieval procedure, and cluster analysis for deep-tissue imaging and, in particular, to breast cancer diagnostics.

Conflicts of interest

There are no conflicts to declare.

Acknowledgements

We acknowledge support from the National Science Foundation (DBI-1455671, ECCS-1509268, CMMI-1826078), AFOSR (FA9550-15-1-0517, FA9550-18-1-0141, FA9550-20-1-0366, FA9550-20-1-0367), Army Research Laboratory (W911NF-17-2-0144), DOD Army Medical Research (W81XWH2010777), ONR (N00014-16-1-2578), NIH (1R01GM127696-01), and the Cancer Prevention and Research Institute of Texas (RP180588).

Notes and References

* Corresponding author; email: yakovlev@tamu.edu.

1 A. J. R. Heck and D. W. Chandler, *Annu. Rev. Phys. Chem.*, 1995, **46**, 335–372.
2 J.-X. Cheng and X. S. Xie, *Science*, 2015, **350**, aaa8870–aaa8870.
3 G. Reich, *Advanced Drug Delivery Reviews*, 2005, **57**, 1109–1143.
4 N. Johnsson and K. Johnsson, *ACS Chem. Biol.*, 2007, **2**, 31–38.
5 C. L. Evans and X. S. Xie, *Annual Rev. Anal. Chem.*, 2008, **1**, 883–909.
6 B. G. Saar, L. R. Contreras-Rojas, X. S. Xie and R. H. Guy, *Molecular Pharmaceutics*, 2011, **8**, 969–975.
7 C. H. Camp and M. T. Cicerone, *Nat. Photonics*, 2015, **9**, 295–305.
8 *Visualizing Chemistry: The Progress and Promise of Advanced Chemical Imaging*, National Academies Press, Washington, D.C., 2006.
9 American Cancer Society, *Available online at http://www.cancer.org/acs/groups/content/@editorial/documents/document/acspc-044552.pdf.*
10 L. Harris, H. Fritsche, R. Mennel, L. Norton, P. Ravdin, S. Taube, M. R. Somerfield, D. F. Hayes and R. C. Bast, *Journal of Clinical Oncology*, 2007, **25**, 5287–5312.
11 E. A. Sickles, *Radiology*, 1986, **160**, 289–293.
12 L. Frappart, M. Boudeulle, J. Boumendil, H. C. Lin, I. Martinon, C. Palayer, Y. Mallet-Guy, D. Raudrant, A. Bremond, Y. Rochet and J. Feroldi, *Human Pathology*, 1984, **15**, 880–889.
13 L. Frappart, I. Remy, H. C. Lin, A. Bremond, D. Raudrant, B. Grousson and J. L. Vauzelle, *Vichows Archiv A Pathol Anat*, 1987, **410**, 179–187.
14 E. Warner, D. B. Plewes, R. S. Shumak, G. C. Catzavelos, L. S. Di Prospero, M. J. Yaffe, V. Goel, E. Ramsay, P. L. Chart, D. E. C. Cole, G. A. Taylor, M. Cutrara, T. H. Samuels, J. P. Murphy, J. M. Murphy and S. A. Narod, *JCO*, 2001, **19**, 3524–3531.
15 M. T. Mandelson, *Journal of the National Cancer Institute*, 2000, **92**, 1081–1087.
16 P. C. Gøtzsche and O. Olsen, *The Lancet*, 2000, **355**, 129–134.
17 F. M. Hall, J. M. Storella, D. Z. Silverstone and G. Wyshak, *Radiology*, 1988, **167**, 353–358.
18 M. E. Phelps, *Proceedings of the National Academy of Sciences*, 2000, **97**, 9226–9233.
19 A. Coulthard and R. Warren, *Breast MRI in practice*, Dunitz, London, 2002.
20 N. Avril, C. A. Rosé, M. Schelling, J. Dose, W. Kuhn, S. Bense, W. Weber, S. Ziegler, H. Graeff and M. Schwaiger, *JCO*, 2000, **18**, 3495–3502.
21 R. Manoharan, K. Shafer, L. Perelman, J. Wu, K. Chen, G. Deinum, M. Fitzmaurice, J. Myles, J. Crowe, R. R. Dasari and M. S. Feld, *Photochem. Photobiol.*, 1998, **67**, 15–22.
22 A. S. Haka, K. E. Shafer-Peltier, M. Fitzmaurice, J. Crowe, R. R. Dasari and M. S. Feld, *Proceedings of the National Academy of Sciences*, 2005, **102**, 12371–12376.
23 R. Weissleder and M. J. Pittet, *Nature*, 2008, **452**, 580–589.
24 P. K. Gupta, S. K. Majumder and A. Uppal, *Lasers Surg Med*, 1997, **21**, 417–422.
25 M. M. Mariani, L. J. Maccoux, C. Matthäus, M. Diem, J. G. Hengstler and V. Deckert, *Anal. Chem.*, 2010, **82**, 4259–4263.
26 W. G. Wang, J. B. Wyckoff, V. C. Frohlich, Y. Oleynikov, S. Huttelmaier, J. Zavadil, L. Cermak, E. P. Bottinger, R. H. Singer, J. G. White, J. E. Segall and J. S. Condeelis, *Cancer Research*, 2002, **62**, 6278–6288.
27 G. I. Petrov, R. Arora, V. V. Yakovlev, X. Wang, A. V. Sokolov and M. O. Scully, *Proc. Natl. Acad. Sci. U. S. A.*, 2007, **104**, 7776–7779.
28 J. R. Lakowicz, *Principles of fluorescence spectroscopy*, Springer, New York, 3rd ed., 2006.
29 V. V. Krishnamachari and E. O. Potma, *J. Opt. Soc. Am. A-Opt. Image Sci. Vis.*, 2007, **24**, 1138–1147.
30 A. Zumbusch, G. R. Holtom and X. S. Xie, *Phys. Rev. Lett.*, 1999, **82**, 4142–4145.
31 J.-X. Cheng and X. S. Xie, *J. Phys. Chem. B*, 2004, **108**, 827–840.

32 E. O. Potma, C. L. Evans and X. S. Xie, *Opt. Lett.*, 2006, **31**, 241–243.
33 E. M. Vartiainen, H. A. Rinia, M. Müller and M. Bonn, *Opt. Express*, 2006, **14**, 3622.
34 J. X. Cheng, L. D. Book and X. S. Xie, *Opt. Lett.*, 2001, **26**, 1341–1343.
35 T. A. H. M. Scholten, G. W. Lucassen, F. F. M. De Mul and J. Greve, *Appl. Opt.*, 1988, **27**, 3225.
36 J. P. Ogilvie, M. Cui, D. Pestov, A. V. Sokolov and M. O. Scully, *Molecular Physics*, 2008, **106**, 587–594.
37 A. Volkmer, J.-X. Cheng and X. Sunney Xie, *Phys. Rev. Lett.*, 2001, **87**, 023901.
38 M. Okuno, H. Kano, P. Leproux, V. Couderc, J. P. R. Day, M. Bonn and H. Hamaguchi, *Angew. Chem.-Int. Edit.*, 2010, **49**, 6773–6777.
39 M. Cicerone, *Current Opinion in Chemical Biology*, 2016, **33**, 179–185.
40 E. M. Vartiainen, *J. Opt. Soc. Am. B*, 1992, **9**, 1209.
41 R. Arora, G. I. Petrov, V. V. Yakovlev and M. O. Scully, *Proc. Natl. Acad. Sci. U. S. A.*, 2012, **109**, 1151–1153.
42 R. Arora, G. I. Petrov and V. V. Yakovlev, *J. Mod. Opt.*, 2008, **55**, 3237–3254.
43 V. V. Yakovlev, *J. Raman Spectrosc.*, 2003, **34**, 957–964.
44 B. G. Saar, C. W. Freudiger, J. Reichman, C. M. Stanley, G. R. Holtom and X. S. Xie, *Science*, 2010, **330**, 1368–1370.
45 G. I. Petrov, V. V. Yakovlev and N. I. Minkovski, *Opt. Commun.*, 2004, **229**, 441–445.
46 L. J. Kong, M. B. Ji, G. R. Holtom, D. Fu, C. W. Freudiger and X. S. Xie, *Opt. Lett.*, 2013, **38**, 145–147.
47 Z. Meng, G. I. Petrov and V. V. Yakovlev, *Sci Rep*, 2016, **6**, 20017.
48 G. I. Petrov, Z. K. Meng and V. V. Yakovlev, *Opt. Express*, 2015, **23**, 24669–24674.
49 T. Wang and C. Xu, *Optica*, 2020, **7**, 947.
50 R. Arora, G. I. Petrov, J. A. Liu and V. V. Yakovlev, *Journal of Biomedical Optics*, 2011, **16**, 11.
51 Y. J. Shen, A. A. Voronin, A. M. Zheltikov, S. P. O'Connor, V. V. Yakovlev, A. V. Sokolov and M. O. Scully, *Sci Rep*, 2018, **8**, 12.
52 B. H. Hokr, J. N. Bixler, G. Elpers, B. Zollars, R. J. Thomas, V. V. Yakovlev and M. O. Scully, *Opt. Express*, 2015, **23**, 8699–8705.
53 J. N. Bixler, Hokr, B. H., Oian, C. A., Noojin, G. D., Thomas, R. J. and Yakovlev, V. V., *arXiv*, 2017, **1509**, 08022.
54 J. N. Bixler, B. H. Hokr, M. L. Denton, G. D. Noojin, A. D. Shingledecker, H. T. Beier, R. J. Thomas, B. A. Rockwell and V. V. Yakovlev, *Journal of Biomedical Optics*, 2014, **19**, 3.
55 P. Lasch, W. Haensch, D. Naumann and M. Diem, *Biochimica et Biophysica Acta (BBA) - Molecular Basis of Disease*, 2004, **1688**, 176–186.
56 R. Arora, G. I. Petrov, V. V. Yakovlev and M. O. Scully, *Analytical Chemistry*, 2014, **86**, 1445–1451.
57 C. G. Kontoyannis, N. Ch. Bouropoulos and P. G. Koutsoukos, *Appl Spectrosc*, 1997, **51**, 64–67.
58 D. C. O'Shea, M. L. Bartlett and R. A. Young, *Archives of Oral Biology*, 1974, **19**, 995–1006.
59 R. Arora, G. I. Petrov, G. D. Noojin, P. A. Thomas, M. L. Denton, B. A. Rockwell, R. J. Thomas and V. V. Yakovlev, *J. Mod. Opt.*, 2011, **58**, 1914–1921.
60 J. V. Thompson, B. H. Hokr and V. V. Yakovlev, *J. Mod. Opt.*, 2016, **63**, 80–84.
61 J. V. Thompson, G. A. Throckmorton, B. H. Hokr and V. V. Yakovlev, *Opt. Lett.*, 2016, **41**, 1769–1772.
62 J. H. Park, S.-W. Lee, E. S. Lee and J. Y. Lee, *Opt. Express*, 2014, **22**, 9854–9870.